JOURNAL OF SPACECRAFT AND ROCKETS
Vol. 38, No. 5, September–October 2001

X-33 Computational Aeroheating Predictions and Comparisons with Experimental Data

Brian R. Hollis,* Thomas J. Horvath,† Scott A. Berry,† H. Harris Hamilton II,‡
Richard A. Thompson,† and Stephen J. Alter§
NASA Langley Research Center, Hampton, Virginia 23681

A computational hypersonic aeroheating study conducted at the NASA Langley Research Center to support development of the X-33 thermal protection system is detailed. In this research, laminar and turbulent aeroheating predictions were generated at wind-tunnel test conditions using two finite volume, Navier–Stokes solvers and a coupled inviscid-solver/boundary-layer-code engineering method. The wind-tunnel computations were performed at Mach 6 for angles of attack of 20–40 deg. Laminar heating distribution comparisons between the predictions and wind-tunnel data were generally within ±10% for the Navier–Stokes method and ±25% for the engineering code method, whereas turbulent computations were within ±20% of the data. Laminar aeroheating computations were also performed at flight conditions using the two Navier–Stokes solvers. Flight-case results from the two Navier–Stokes codes were found to agree to within less than ±10%.

Nomenclature

C_{CP}	=	constant in Baldwin–Lomax model (1.6)
C_{KLEB}	=	constant in Baldwin–Lomax model (0.3)
D	=	damping factor in Baldwin–Lomax model
F	=	vorticity function in Baldwin–Lomax model
F_{KLEB}	=	Klebanoff's intermittency factor
H	=	enthalpy, J/kg
h	=	heat transfer coefficient, $h = \dot{q}/(H_{aw} - H_w)$, kg/(m^2 · s)
h_{FR}	=	Fay–Riddell heating coefficient, kg/(m^2 · s)
K_v	=	von Kármán constant (0.4)
L	=	reference length, m
l	=	mixing length, m
M	=	Mach number
n	=	normal distance from wall, m
n^+	=	normalized coordinate parameter
p	=	pressure, N/m^2
$\dot{q}$	=	heat transfer rate, W/m^2
Re	=	Reynolds number
T	=	temperature, K
U_∞	=	freestream velocity, m/s
X, Y, Z	=	coordinate system, m
α	=	angle of attack, deg
μ	=	laminar viscosity, kg/(m · s)
$\mu_{t,i}$	=	inner-layer eddy viscosity, kg/(m · s)
$\mu_{t,o}$	=	outer-layer eddy viscosity, kg/(m · s)
ρ	=	density, kg/m^3
τ	=	shear stress, kg/(m · s^2)
Ω	=	damping variable in Baldwin–Lomax model
ω	=	vorticity, 1/s

Subscripts

w	=	wall
∞	=	freestream

Received 23 July 1999; revision received 6 November 2000; accepted for publication 5 February 2001.

*Aerospace Technologist, Aerothermodynamics Branch, Aerodynamics, Aerothermodynamics, and Acoustics Competency. Member AIAA.

†Aerospace Technologist, Aerothermodynamics Branch, Aerodynamics, Aerothermodynamics, and Acoustics Competency.

‡Aerospace Technologist, Aerothermodynamics Branch, Aerodynamics, Aerothermodynamics, and Acoustics Competency. Associate Fellow AIAA.

§Aerospace Technologist, Aerothermodynamics Branch, Aerodynamics, Aerothermodynamics, and Acoustics Competency. Senior Member AIAA.

Introduction

THE X-33 vehicle will be a subscale technology demonstrator for an economical, full-scale, single-stage-to-orbitreusable launch vehicle (SSTO-RLV). It is intended to prove the feasibility of the SSTO-RLV concept through demonstration of key design and operational aspects of the vehicle. Additional background on the X-33 program is provided in Refs. 1–5.

As part of an industry/government partnership in the X-33 program, the NASA Langley Research Center (LaRC) was tasked to provide aerodynamic and aeroheating results to support the design and development of the vehicle. Earlier results of this work have been presented by Hamilton et al.[6] and Thompson et al.[7] The current research program is detailed in companion papers by Berry et al.,[8] Hollis et al.,[9] Horvath et al.,[10] Murphy et al.,[11] and Thompson.[12]

In the present paper, laminar and turbulent Navier–Stokes and boundary-layer engineering code predictions for the aeroheating environment of the X-33 at hypersonic flight and wind-tunnel test conditions are presented and compared with experimental data from Refs. 8 and 10. Computational issues including grid resolution and adaption, turbulence modeling, and inviscid flux formulations are also discussed.

X-33 Geometry

The computational results presented are based on the 604B0002F configuration of the Lockheed Martin X-33 vehicle, which is commonly referred to as the F-Loft, Rev-F configuration. A brief history of the X-33 configuration evolution through phase II of the program is presented in Ref. 10. The current F-Loft, Rev-F configuration (Fig. 1) is a lifting-body delta planform with twin vertical tails, canted fins, and body flaps. The body length is 19.3 m (63.2 ft) from the nose to the end of the engine module, and the span across the canted fins is 8.11 m (36.6 ft). The canted fins have a dihedral of 20 deg and a −8.58-deg incidence angle. Although some slight changes in the X-33 configuration have occurred since this research began, they were not of enough significance to warrant updating the computational modeling of the geometry.

Computational Methods

Numerical Algorithms

Computational predictions for comparison with the wind-tunnel aeroheating test data were generated using two Navier–Stokes solvers, GASP[13] and LAURA,[14,15] and an engineering method in which the LATCH[16] boundary-layer code and an inviscid solution from the LAURA code were employed to compute surface heating distributions. Flight predictions were generated using both GASP and LAURA.

The GASP code is a three-dimensional, finite volume Navier–Stokes solver that incorporates numerous flux formulations, thermochemical models, turbulence models, and time-integration methods. A perfect-gas air model was used for the wind-tunnel test cases discussed in this paper, and an equilibrium air model was used for the trajectory cases. The Jacobi scheme was used for time integration. Full viscous terms were retained for all three directions and modeled with second-order central differences. As will be detailed in the "Flux Splitting" section, a third-order, upwind-biased, min–mod limited scheme, which consisted of a Roe[17] flux formulation in the body-normal direction and a Van Leer[18] formulation in the other two directions, was employed to represent the inviscid fluxes. The turbulent computations were performed using the algebraic Baldwin–Lomax[19] model with modifications to the damping term.

The LAURA code is a three-dimensional Navier–Stokes solver based on a point-relaxation scheme and Roe[17] averaging with Yee's[20] symmetric total variation diminishing limiter for inviscid fluxes. The code includes perfect-gas, equilibrium, and nonequilibrium air models. For the present work, viscous and inviscid solutions (for use with LATCH) for the wind-tunnel cases were generated using the perfect-gas air model. Trajectory computations were also performed using a nonequilibrium air model.

The LATCH code is a three-dimensional boundary-layer code based on the axisymmetric analog[21] for general three-dimensional boundary layers. An approximate integral heating method[22] is used to compute the heating rates along three-dimensional inviscid streamlines. The inviscid streamlines must be supplied from separate, three-dimensional inviscid flowfield computations, which were generated with the LAURA code in this work.

Boundary Conditions and Thermochemical Models

Freestream conditions for the Mach 6 wind-tunnel cases were taken from those of aeroheating tests[8,10] conducted in the LaRC 20-Inch Mach 6 Air Tunnel. This facility is described in Ref. 23. Freestream conditions for these cases are listed in Table 1. The wall boundary condition for the computations was fixed at a uniform ambient (300-K) temperature. This approximation is valid because an aeroheating run in this tunnel is of short enough duration such that the increase in model surface temperature can be neglected.

Freestream conditions for the flight cases were taken from the Michael 9A-8 trajectory, which was the current design trajectory at the time of this research. This trajectory is shown in Fig. 2, and the freestream conditions for these cases are listed in Table 1. For all flight cases, a radiative equilibrium wall temperature with an emissivity of 0.85 was specified.

All wind-tunnel cases were computed using a perfect-gas air model. Flight cases were computed with GASP using an equilibrium air model and with LAURA using a nonequilibrium air model with a fully catalytic wall boundary condition. However, given the relatively low Mach numbers of the flight cases, there should be little difference in results computed using either equilibrium or nonequilibrium models.

Table 1 Flow conditions for wind-tunnel and flight cases

Case	Mach	T_∞, K	ρ_∞, kg/m^3	U_∞, m/s	Re_∞, 1/m	α, deg
20-Inch Mach 6 Air Tunnel (LAURA)	5.95	62.6	3.24*e*−2	943.0	6.80*e*6	24, 36
20-Inch Mach 6 Air Tunnel (GASP)	5.99	62.1	6.28*e*−2	945.1	1.31*e*7	20, 30, 40
Flight case 1 (Michael 9A-8)	8.82	265.9	7.07*e*−4	2887.3	1.07*e*5	10
Flight case 2 (Michael 9A-8)	8.89	252.1	3.87*e*−4	2833.5	5.97*e*4	30

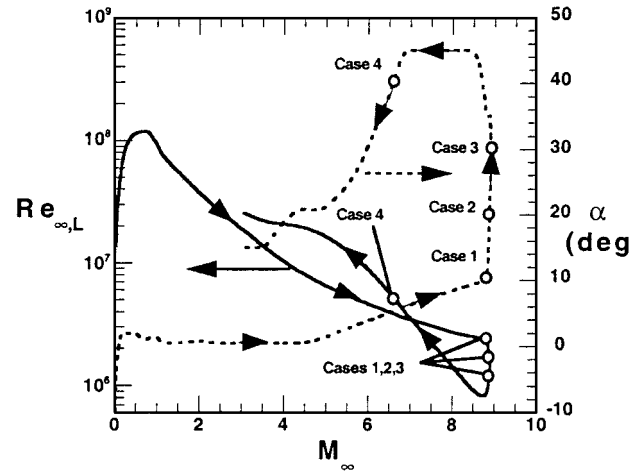

Fig. 2 Points for computations along Michael 9A-8 trajectory.

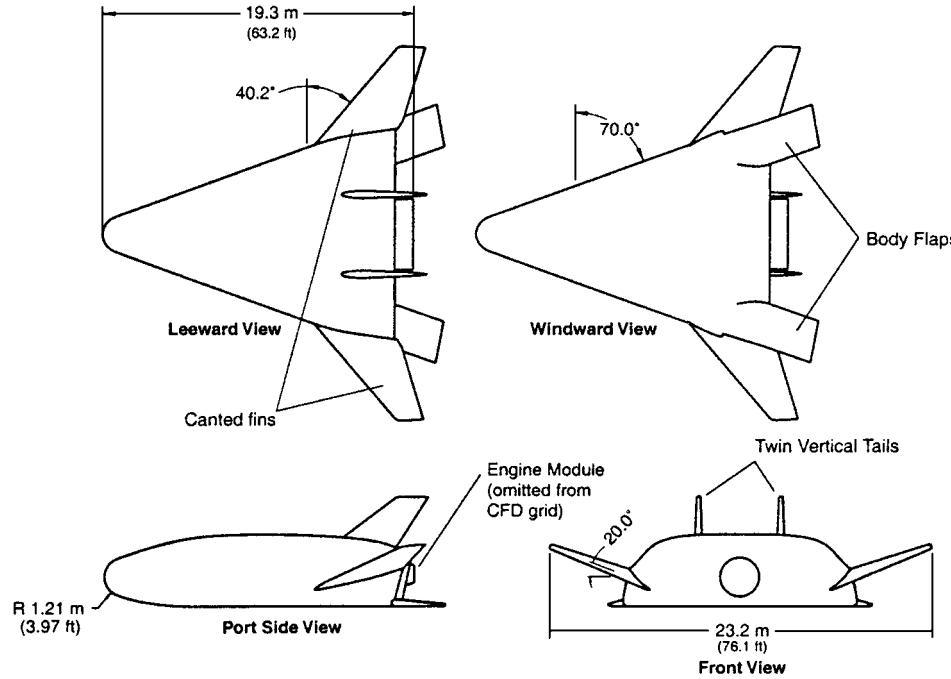

Fig. 1 X-33 F-Loft, Rev-F vehicle.

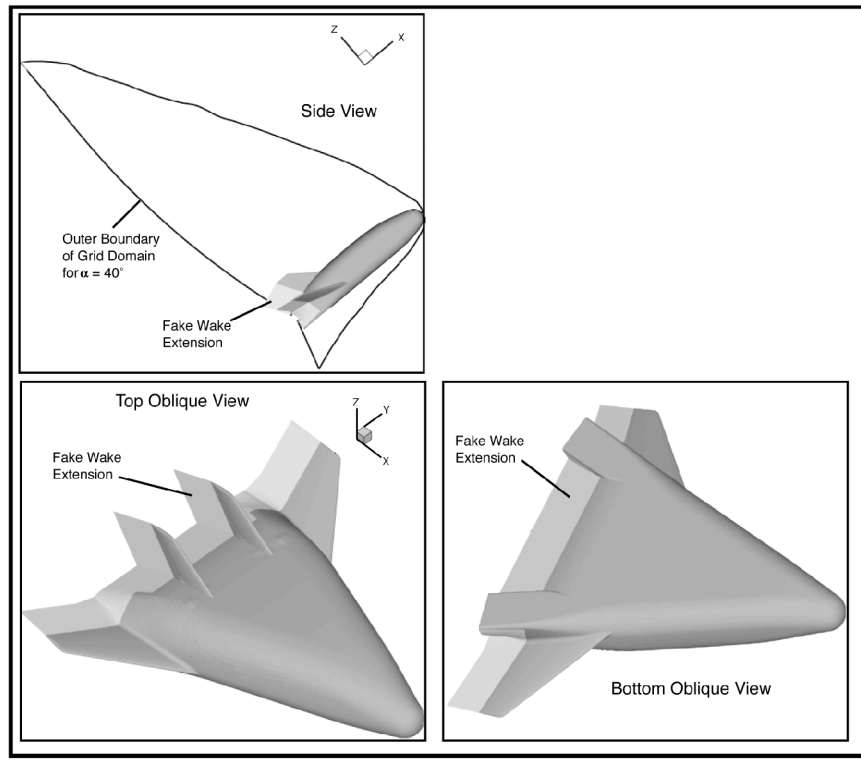

Fig. 3 X-33 Computational geometry with fake-wake extension.

Grid Generation and Adaption

The laminar GASP flowfield computations were performed on a $(127 \times 181 \times 65)$ point, single-block, half-body grid[24] (Fig. 3), whereas the laminar LAURA computations were performed on a $(253 \times 181 \times 65)$ point grid. Turbulent GASP computations were performed on a $(127 \times 181 \times 128)$ point grid. For the wind-tunnel cases, a grid scale of 1.32% that of the full-size X-33 vehicle was chosen to match that of the wind-tunnel models tested in Refs. 8 and 10. On this scale, the vehicle length is 0.254 m (10.0 in.) from the nose of the vehicle to the end of the engine module. The engine module and wake were not included in this grid, and a fake-wake, solid-body representation was employed for the regions between the canted fins and the end of the body flaps and between the body flaps. The exclusion of the wake from the grid is expected to have a negligible effect on the computations, except perhaps at the end of the fuselage because only local surface quantities, that is, convective heating and pressure, are of interest, as opposed to integrated aerodynamic quantities such as the pitching moment.

For each angle-of-attack case, grid adaption was performed to align the outer domain of the grid with the bow shock and to cluster grid points within the wall boundary layer. Typically, the outer boundary was adjusted so that the shock was located at approximately 80% of the normal distance between the wall and outer grid boundary. Approximately 50% of the normal grid points were clustered within the wall boundary layer, and the wall cell Reynolds number was set in the range of 10–20. The scheme employed to perform these manipulations is based on Ref. 15. When necessary, additional grid quality refinement and smoothing was performed using the Volume Grid Manipulation code.[25]

Flux Splitting

As previously mentioned, the GASP code incorporates a number of different flux functions including the Roe,[17] Van Leer,[18] and Roe–Harten[26] schemes. Several test cases were computed to determine the suitability of these schemes for viscous hypersonic flowfield computations. The test cases were Van Leer flux in all three computational directions (VLVLVL), Roe flux in the normal direction with Van Leer in the other two directions (VLVLRo), Roe–Harten flux in the normal direction with Van Leer in the other two directions (VLVLRH), Roe flux in all directions (RoRoRo), and Roe–Harten

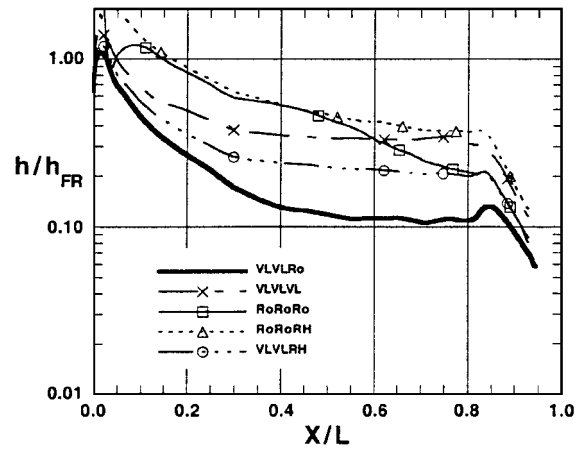

Fig. 4 Effect of flux formulation on centerline heating distribution, $\alpha = 40$ deg.

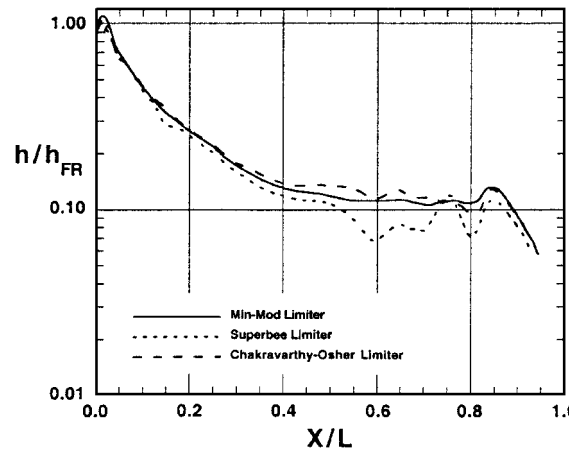

Fig. 5 Effect of TVD limiter on centerline heating distribution, $\alpha = 40$ deg.

flux in the normal direction with the Roe scheme in the other two directions (RoRoRH). For all test cases, a third-order flux formulation with a min–mod total variation diminishing (TVD) limiter was employed. The freestream conditions for these test cases were those of the Mach 6, $Re_\infty = 1.31 \times 10^7$/m ($4.0 \times 10^6$/ft) wind-tunnel case with $\alpha = 40$ deg.

Centerline heating predictions generated using each of these methods are shown in Fig. 4, and as can be seen in Fig. 4, the choice of flux functions has a large influence on surface heating computations. The use of Roe's flux in the normal direction is known to produce numerical instabilities around the stagnation region, which can be seen in the discontinuous heating distribution near the nose for the RoRoRo case. Harten's correction in the RoRoRH method dampens out the numerical instability, but introduces excessive dissipation, which elevates the heating rates. (Note that the Roe–Harten implementation in GASP is not the same as that in LAURA; in LAURA, the Harten entropy correction has been further modified to produce less dissipation, as documented in Ref. 15.) The three cases run with Van Leer's flux (VLVLVL, VLVLRH, and VLVLRo) all produced smooth solutions with varying amounts of numerical dissipation depending on the normal-direction flux. Of the options employed, the case with the Roe flux in the normal direction and Van Leer in the other directions (VLVLRo) produced the smoothest distribution with the least dissipation, that is, produced the lowest heating rates, and is, thus, assumed to be the best solution method of the options available in GASP.

The VLVLRo method was used for all subsequent computations, and its accuracy will be demonstrated in a later section where heating predictions generated using the VLVLRo method are compared with experimental data. In contrast, the much more dissipative VLVLVL scheme was employed in Ref. 27 to generate a design aeroheating database for the X-33 vehicle, which illustrates the need for independent verification of critical vehicle design data either through code-to-code comparisons, code-to-experiment comparisons, or both.

After establishing that the VLVLRo method produced the best results, the influence of the TVD limiters on the solution was investigated. Additional cases were run using the VLVLRo scheme with the Superbee[28] and Chakravarthy–Osher[29] limiters in place of the min–mod limiter in the body-normal direction. As shown in Fig. 5, the magnitude of the centerline heating distributions showed much less sensitivity to the limiter than was observed for the flux formulations. However, both the Superbee and Chakravarthy–Osher limited solutions showed a lack of smoothness along the body. Therefore, it was concluded that the VLVLRo scheme with min–mod limiting produced the best results.

Grid Resolution

Laminar GASP computations for the wind-tunnel cases presented were generated with the VLVLRo scheme and the min–mod limiter on a ($127 \times 181 \times 65$) point grid. This grid point density was determined to be sufficient through a grid resolution study, which is shown in Figs. 6–9. LAURA computations were performed on a higher resolution ($253 \times 181 \times 65$) grid before this study. In Figs. 6–9, surface heating distributions computed on the ($127 \times 181 \times 65$) point grid as well as on grids with one-half and one-quarter the point density of the original grid are shown along the centerline of the vehicle and at three axial stations. The computed heating distributions were found to decrease by approximately 10–20% between the coarse grid

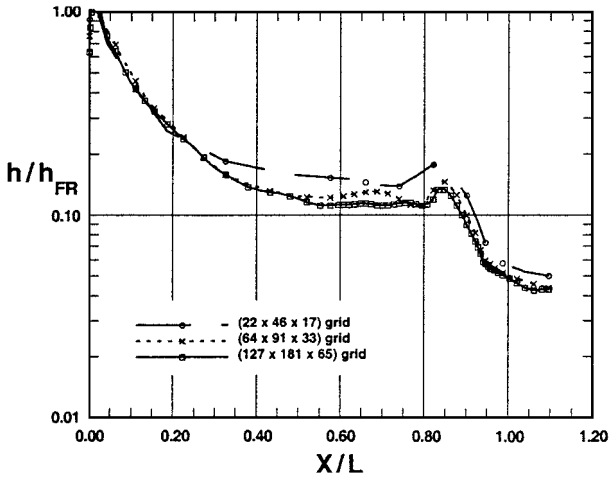

Fig. 6 Grid resolution effects on computed centerline heating distribution, $\alpha = 30$ deg.

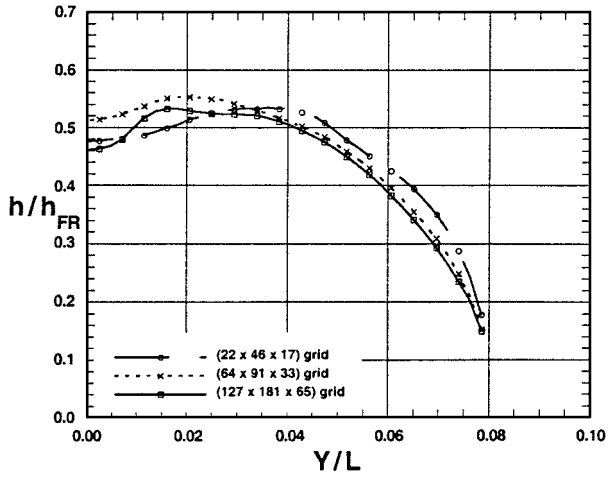

Fig. 7 Grid resolution effects on computed axial heating distribution at $X/L = 0.1$ and $\alpha = 30$ deg.

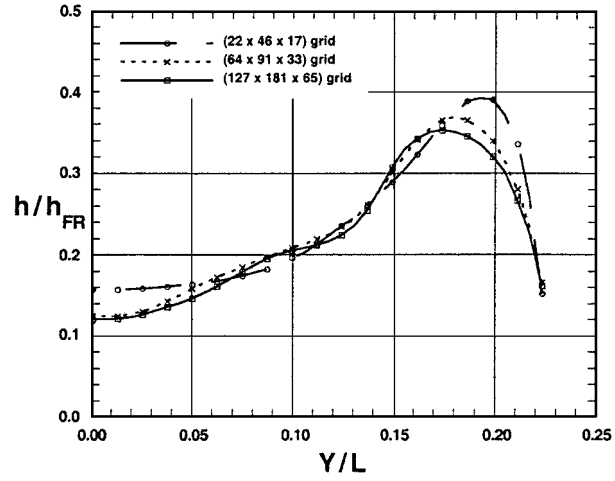

Fig. 8 Grid resolution effects on computed axial heating distribution at $X/L = 0.5$ and $\alpha = 30$ deg.

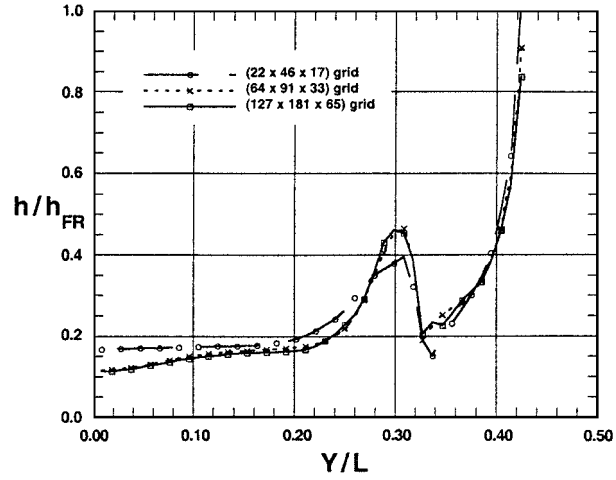

Fig. 9 Grid resolution effects on computed axial heating distribution at $X/L = 0.8$ and $\alpha = 30$ deg.

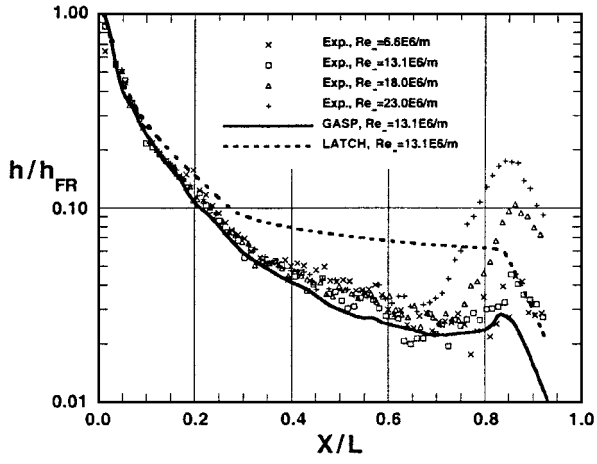

Fig. 10 Windward centerline heating data comparison with laminar computations at $\alpha = 20$ deg.

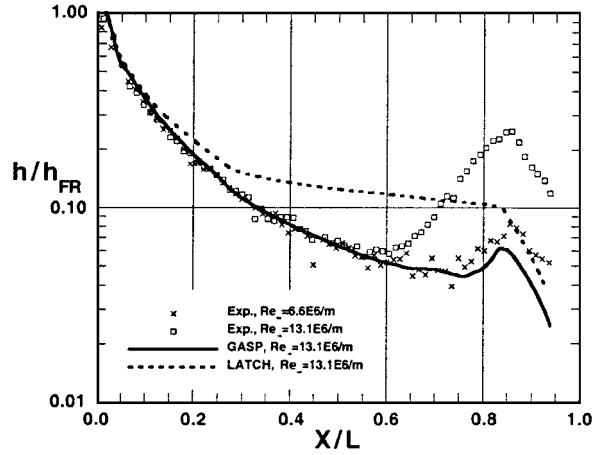

Fig. 11 Windward centerline heating data comparison with laminar computations at $\alpha = 30$ deg.

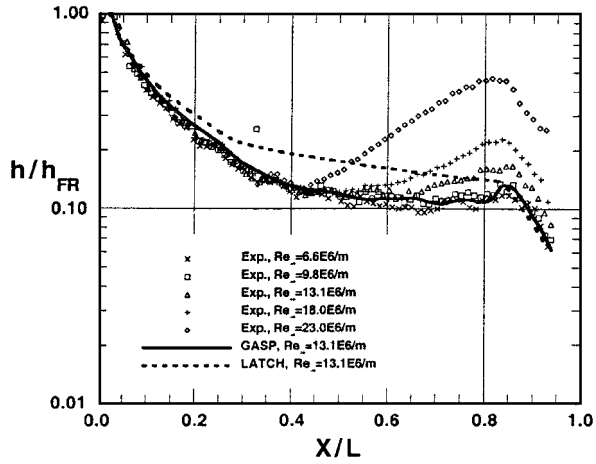

Fig. 12 Windward centerline heating data comparison with laminar computations at $\alpha = 40$ deg.

and the intermediate grid, but decreased by only 5–8% between the intermediate and fine grids. These results suggest that the errors due to grid resolution for computations on the $(127 \times 181 \times 65)$ point grid are no more than 2–3%. Furthermore, the fairly good accuracy of the results obtained on the intermediate $(64 \times 91 \times 33)$ grid suggests that preliminary design computations for a vehicle such as the X-33 could be performed rapidly on a coarser grid and that only the final design computations need be performed on a fine grid. Finally, because it can be expected that turbulent computations would be more sensitive to grid resolution than the laminar computations, the normal-point grid resolution was doubled for the turbulent cases to produce a $(127 \times 181 \times 129)$ point grid.

Experiment Background

The experimental aeroheating tests that complement this computational study are presented in detail in Refs. 8 and 10. The goal of these tests was to define the overall aeroheating environment of the X-33 vehicle and to examine the effects of discrete and distributed roughness on boundary-layer transition. To date, the aeroheating test program includes over 1100 runs in three different hypersonic wind tunnels. The experimental data referenced in the present work were acquired in the NASA LaRC 20-Inch Mach 6 Air Tunnel. A description of this facility can be found in Ref. 23.

Aeroheating tests in this tunnel were conducted across a range of Reynolds numbers from 3.3×10^6/m (1.0×10^6/ft) to 23.1×10^6/m (7.0×10^6/ft) at angles of attack from 0 to 40 deg with body flap deflections of 0, +10, and +20 deg. Aeroheating image data were obtained in these tests using the two-color, relative intensity, phosphor thermography technique.[30] The image data were then reduced and analyzed using the IHEAT code,[30] and numerical data were extracted from the images at specified lateral and longitudinal stations. Global data produced by the phosphor technique permit the resolution of complex flow phenomena such as transition fronts, vortex structures, and shock interactions. Comparisons of phosphor thermography results with computations have been presented in Refs. 6 and 31.

As discussed in Ref. 30, the accuracy of the phosphor technique is dependent on the temperature rise on the surface of the test model. For the windward-side heating measurements, the accuracy of the phosphor system is estimated to be approximately ±8%, and the overall experimental uncertainty of the heating data due to all factors is estimated to be ±15%. Because the leeside temperature rise is only a few degrees during a test, the experimental uncertainty for leeside heating rates increases to at least ±25%.

Computations for Wind-Tunnel Cases and Comparisons with Experimental Data

Results from GASP, LAURA, and LATCH/LAURA computations will be presented in this section, and comparisons will be made with experimental data. The heating distributions will be presented in terms of the ratio h/h_{FR}. The quantity h_{FR} is a reference heat transfer coefficient, where the wall heating rate $\dot{q}$ is based on Fay–Riddell[32] theory for a hemisphere of the same radius as the nose of X-33 model (1.60 cm), the adiabatic wall enthalpy H_{aw} is assumed to be equal to the total tunnel enthalpy $H_{T,2}$, and the wall enthalpy is computed at an ambient (300-K) wall temperature. Geometric positions are given in nondimensional form, X/L, Y/L, Z/L, where L is the reference length (0.254 m) of the wind-tunnel model.

Laminar Centerline and Axial Cut Comparisons

For a detailed quantitative assessment of the agreement between experimental data and computations, heating distributions were extracted from both sets of data along the centerline of the vehicle and at various axial stations along the body. Laminar GASP and LATCH windward and centerline distributions for angles of attack of 20, 30, and 40 deg are compared with experimental data in Figs. 10–12. Laminar GASP and LATCH distributions for axial stations of $X/L = 0.05$, 0.10, 0.20, 0.32, 0.45, and 0.90 for the $\alpha = 30$ deg case are compared with experimental data in Figs. 13–18. Computed laminar windward centerline distributions from the LAURA code are plotted vs experimental data in Figs. 19 and 20.

In Figs. 10–20 experimental heating distributions extracted from the global heating images using the IHEAT code for Reynolds numbers from 3.3×10^6/m (1.0×10^6/ft) to 23.1×10^6/m (7.0×10^6/ft) are provided for comparison with the computations. In the wind-tunnel tests, natural transition from laminar flow was observed to begin near the end of the X-33 fuselage on the windward surface at freestream Reynolds number of 13.1×10^6/m (4.0×10^6/ft) and higher. Data where transition was produced with boundary-layer trips are also shown.

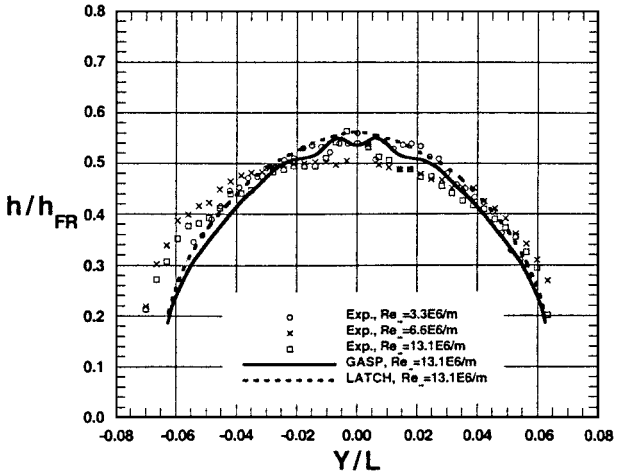

Fig. 13 Axial heating data comparison with laminar computations at $X/L = 0.05$ for $\alpha = 30$ deg.

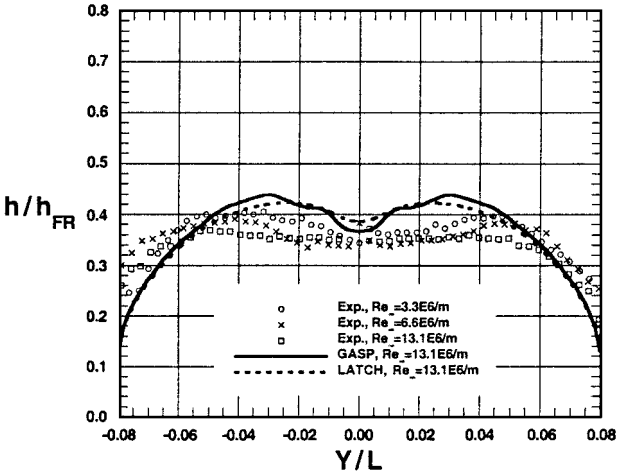

Fig. 14 Axial heating data comparison with laminar computations at $X/L = 0.10$ for $\alpha = 30$ deg.

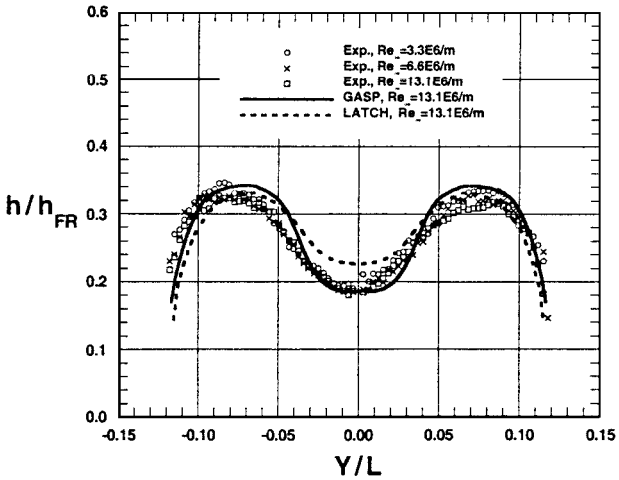

Fig. 15 Axial heating data comparison with laminar computations at $X/L = 0.20$ for $\alpha = 30$ deg.

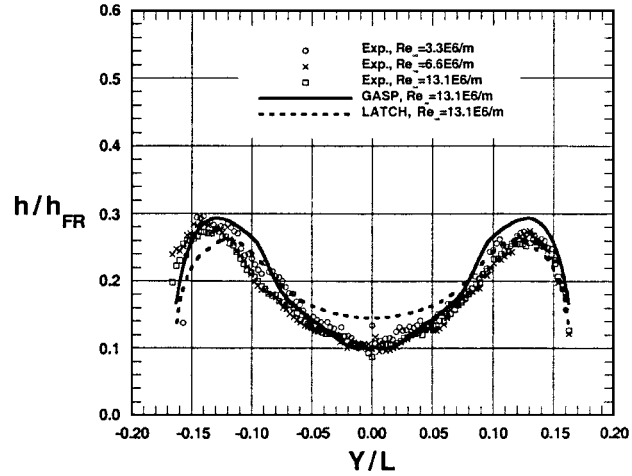

Fig. 16 Axial heating data comparison with laminar computations at $X/L = 0.32$ for $\alpha = 30$ deg.

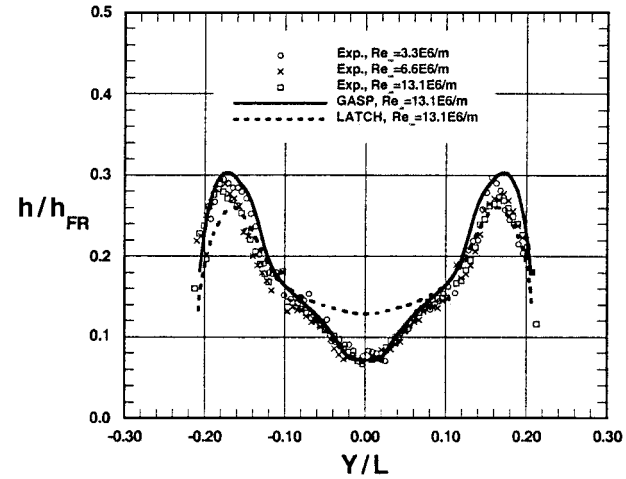

Fig. 17 Axial heating data comparison with laminar computations at $X/L = 0.45$ for $\alpha = 30$ deg.

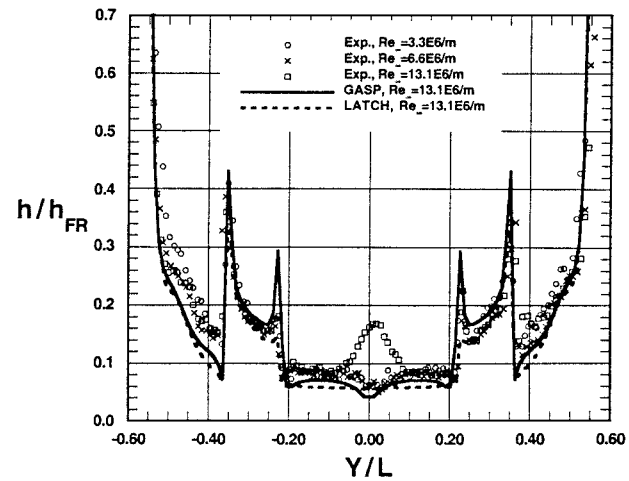

Fig. 18 Axial heating data comparison with laminar computations at $X/L = 0.90$ for $\alpha = 30$ deg.

As shown in Figs. 10–12, the laminar GASP computations and laminar experimental data generally compare to within less than $\pm 10\%$ and agree to within the $\pm 15\%$ experimental uncertainty along the full length of the vehicle at all angles of attack. The LATCH boundary-layer results are in close agreement with the experimental data only along the first third of the vehicle; beyond that point, the LATCH results are substantially higher than wind-tunnel data.

In the windward-surface axial cut comparisons of Figs. 13–18, close agreement between the laminar GASP predictions and experimental data is again observed at each of the axial stations. In the areas along the chines near the nose of the vehicle, the differences between the GASP computations and the data are slightly larger than on the rest of the windward surface (approximately 15%), but are still within the estimated uncertainty. Also note that away from the centerline, the LATCH computations are in much better agreement with both GASP results and the wind-tunnel data and fall within the experimental uncertainty. This result would suggest that

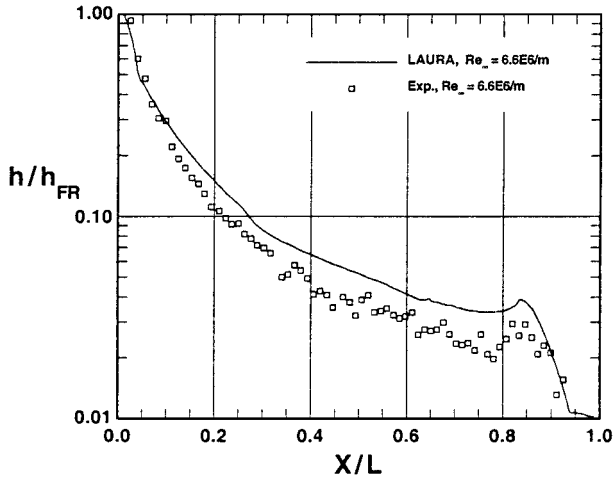

Fig. 19 Windward centerline heating data comparison with laminar computations at $\alpha = 24$ deg.

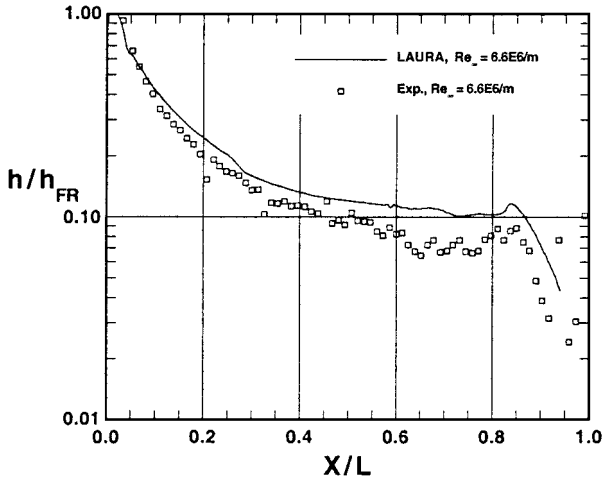

Fig. 20 Windward centerline heating data comparison with laminar computations at $\alpha = 36$ deg.

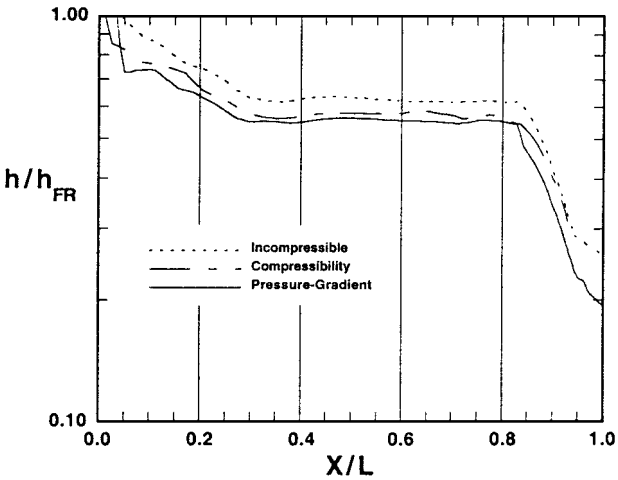

Fig. 21 Comparison of turbulent heating predictions for different forms of Baldwin–Lomax model (Mach 6, $\alpha = 40$ deg wind-tunnel case).

centerline comparisons alone may not provide sufficient information for a complete code validation study.

LAURA windward centerline heating computations (Figs. 19 and 20) also agree with the data to within the experimental uncertainty except near the end of the vehicle at $\alpha = 36$ deg, where the LAURA predictions are slightly higher than the data.

Turbulent Centerline Comparisons

An algebraic turbulence model based on the work of Baldwin and Lomax[19] was employed in this work for all turbulent computations.

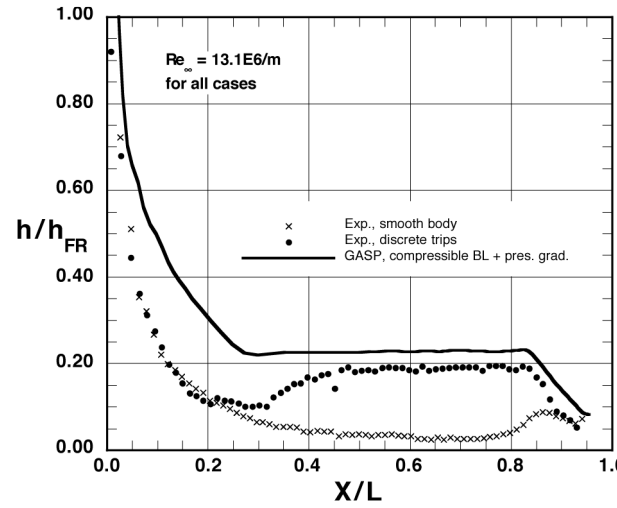

Fig. 22 Windward centerline heating data comparison with turbulent computations at $\alpha = 20$ deg.

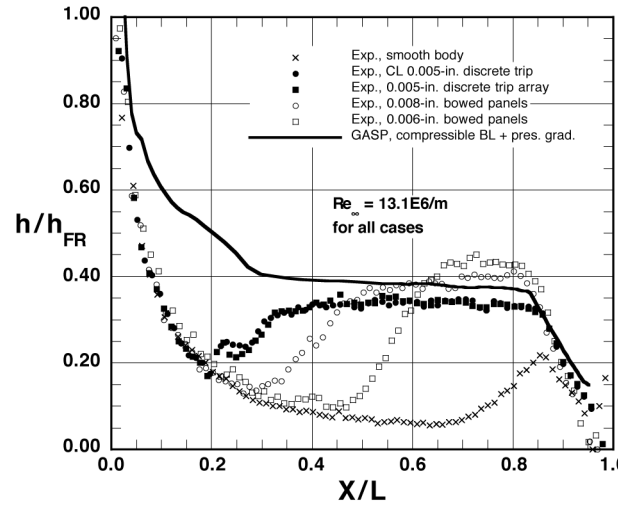

Fig. 23 Windward centerline heating data comparison with turbulent computations at $\alpha = 30$ deg.

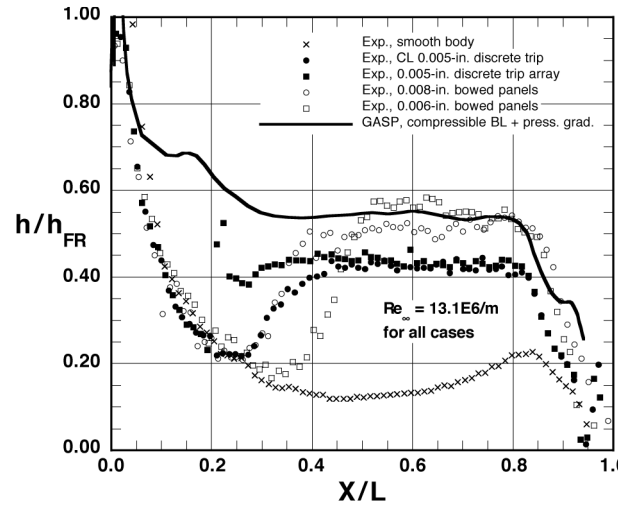

Fig. 24 Windward centerline heating data comparison with turbulent computations at $\alpha = 40$ deg.

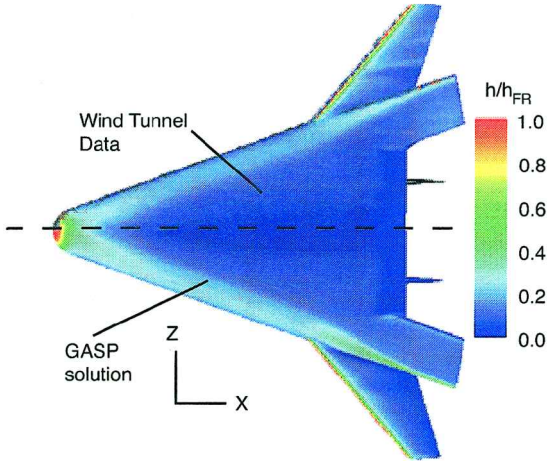

Fig. 25 Global comparison of GASP computation and tunnel data, $\alpha = 20$ deg, windward view.

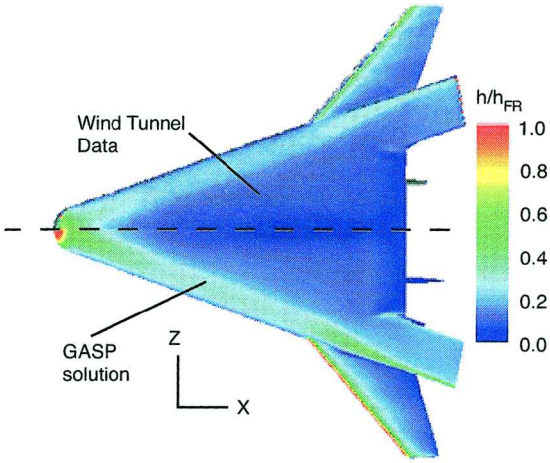

Fig. 26 Global comparison of GASP computation and tunnel data, $\alpha = 30$ deg, windward view.

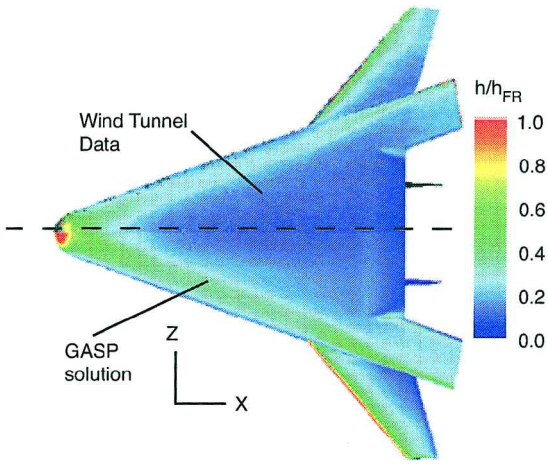

Fig. 27 Global comparison of GASP computation and tunnel data, $\alpha = 40$ deg, windward view.

The Baldwin–Lomax model consists of a two-layer representation of the eddy viscosity, where the inner-layer eddy viscosity is given by

$$\mu_{t,i} = \rho l_{\text{mix}}^2 |\omega| \tag{1}$$

The mixing length l_{mix} is given by

$$l_{\text{mix}} = K_v n D \tag{2}$$

where the von Kármán constant is $K_v = 0.4$. The damping factor is

$$D = 1 - \exp(-n^+/A^+) \tag{3}$$

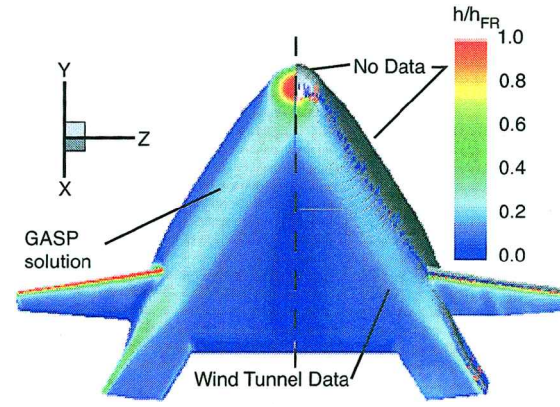

Fig. 28 Global comparison of GASP computation and tunnel data, $\alpha = 20$ deg, front view.

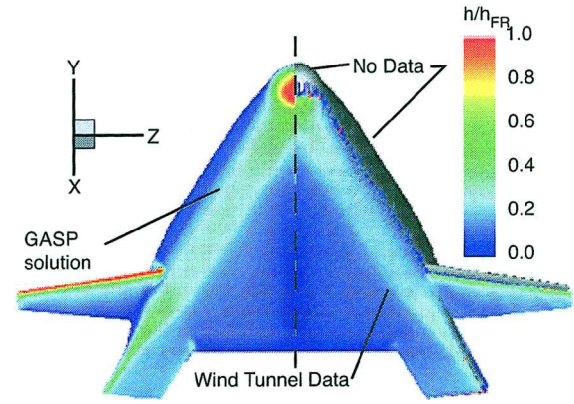

Fig. 29 Global comparison of GASP computation and tunnel data, $\alpha = 30$ deg, front view.

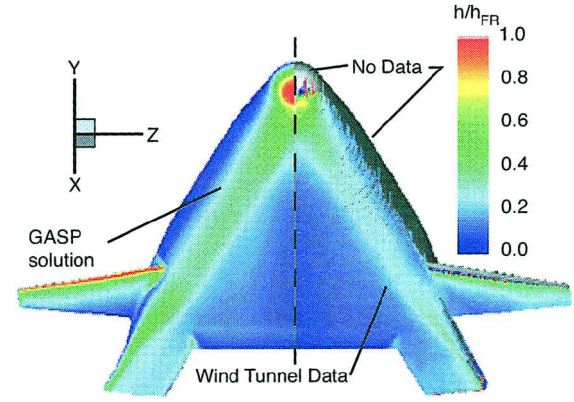

Fig. 30 Global comparison of GASP computation and tunnel data, $\alpha = 40$ deg, front view.

where the normal coordinate parameter is

$$n^+ = n\sqrt{\rho_w \tau_w}/\mu_w \tag{4}$$

with

$$\tau_w = \mu_w |\omega_w| \tag{5}$$

and A^+ is a constant equal to 26. The outer layer viscosity is given by

$$\mu_{t,0} = 0.0168 \rho C_{\text{CP}} F_{\max} n_{\max} F_{\text{KLEB}} \tag{6}$$

where C_{CP} is a constant equal to 1.6, $n_{\max}$ is the location of the maximum $F_{\max}$ (within the boundary layer), of the vorticity function F,

$$F = n|\omega|D \tag{7}$$

and F_{KLEB} is Klebanoff's intermittency factor:

$$F_{KLEB} = \left[1 + 5.5\left(\frac{C_{KLEB}\, n}{n_{max}}\right)^6\right]^{-1} \tag{8}$$

with the constant $C_{KLEB} = 0.3$.

The Baldwin–Lomax model was developed for low-speed, incompressible flow, and so various modifications have been proposed to render it suitable for use in hypersonic flows. The most widely accepted modification is that to account for compressibility by using local property values in the damping term definition instead of wall values:

$$(n^+)_{comp} = \frac{n\sqrt{\rho\tau_w}}{\mu} \tag{9}$$

If a damping variable for the original incompressible Baldwin–Lomax scheme is defined as

$$\Omega_{inc} = n^+/A^+ = (n/26)\sqrt{(\rho_w|\omega_w|)/\mu_w} \tag{10}$$

then the damping variable for the compressible form can be written as

$$\Omega_{comp} = \Omega_{inc}\left[(\sqrt{\rho/\rho_w})(\mu_w/\mu)\right] \tag{11}$$

Another modification,[33,34] which takes into account both compressibility and a streamwise pressure gradient and has been shown to produce good agreement with hypersonic heating data, is given by

$$\Omega_{pres} = \Omega_{inc}\sqrt{(\rho/\rho_w)|(\omega/\omega_w)|[\mu_w(\mu + \mu_t)/\mu^2]} \tag{12}$$

The GASP code was modified to include the form given in Eq. (12), which was used for the turbulent computations in this work. Note that, in an earlier report,[35] the turbulent viscosity was inadvertently omitted from Eq. (12) when modifying GASP, which resulted in significantly lower turbulent heating rates.

A comparison of turbulent centerline heating predictions from these three forms of the Baldwin–Lomax model for the $\alpha = 40$ deg wind-tunnel case is presented in Fig. 21. Note the laminar ($127 \times 181 \times 65$) point grid was employed in this comparison for convenience. The compressible form yields heating rates approximately 10% lower than the incompressible form, whereas the pressure-gradient form produces heating rates approximately 5% lower than the compressibility form.

Centerline heating distributions computed using the pressure-gradient form of the Baldwin–Lomax model for angles of attack of 20, 30, and 40 deg are compared to the wind-tunnel data in Figs. 22–24. These computations were all performed on the ($127 \times 181 \times 128$) point grid. The wind-tunnel results shown[8] include data from smooth models, models on which discrete 0.005-in. trips were placed, and models with simulated bowed thermal protection system panels of various heights near the nose. All experimental data are for $Re_\infty = 13.1 \times 10^6$/m. The smooth model data show transition beginning only near the end of the model. The discrete trips and bowed panels both produced clearly nonlaminar data. However, these two tripping methods produce different levels of heating, and whether or not the data represent a fully developed

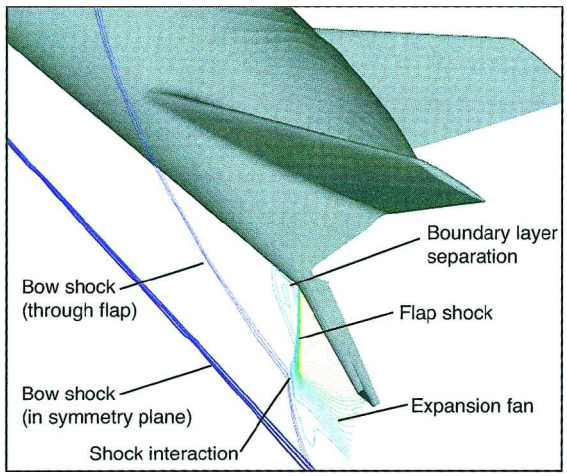

Fig. 31 Pressure contours showing shock–shock interaction for Mach 6, $\alpha = 40$ deg case.

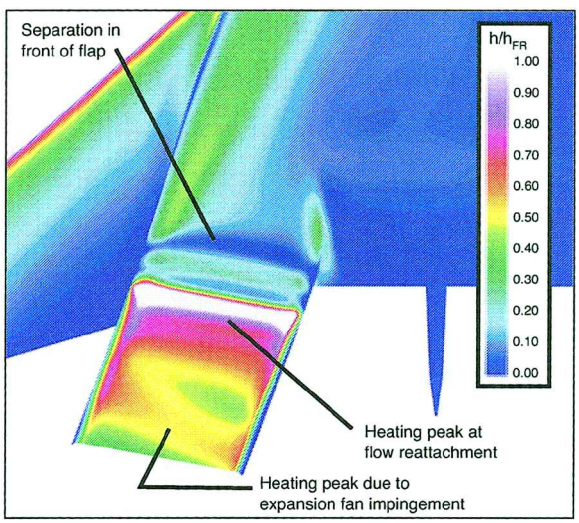

Fig. 32 Heating distribution produced by shock–shock interaction for Mach 6, $\alpha = 40$ deg case.

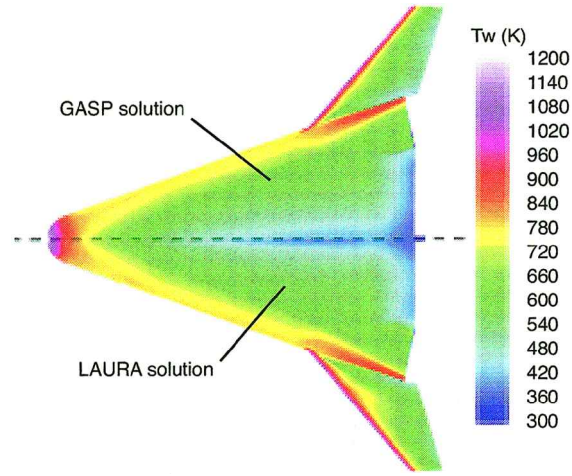

Fig. 33 Computed windward wall temperatures for case 1, peak heating (Mach 8.82, $\alpha = 10$ deg).

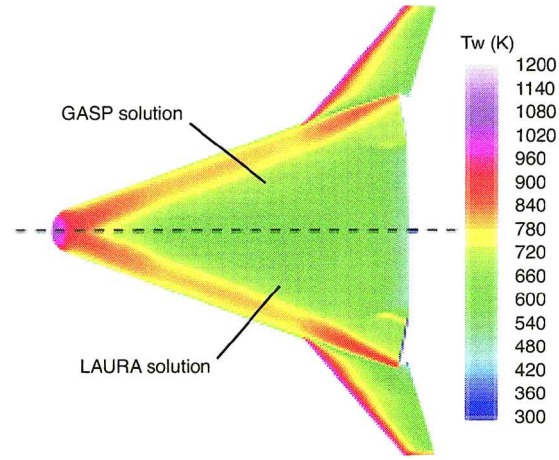

Fig. 34 Computed windward wall temperatures for case 2 (Mach 8.87, $\alpha = 20$ deg).

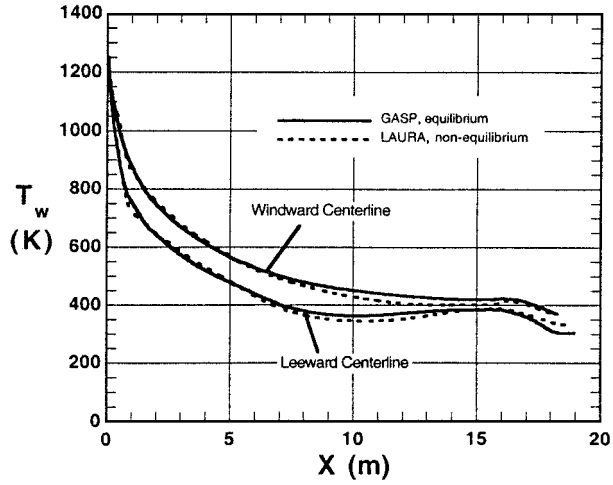

Fig. 35 Computed centerline wall temperatures for flight case 1, peak heating (Mach 8.82, $\alpha = 10$ deg).

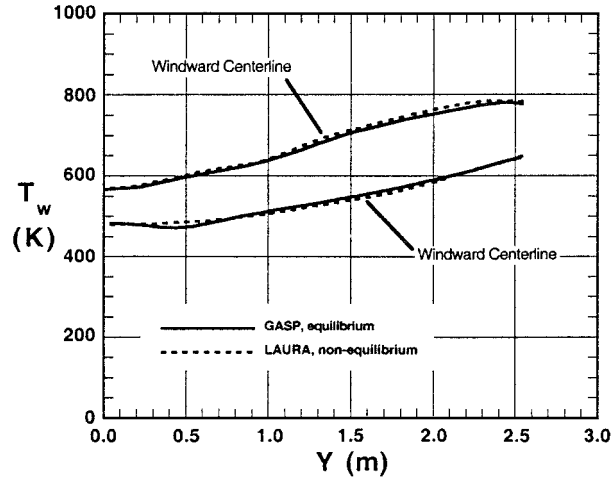

Fig. 36 Computed wall temperatures at $X = 5.0$ m (after nose region) for flight case 1, peak heating (Mach 8.82, $\alpha = 10$ deg).

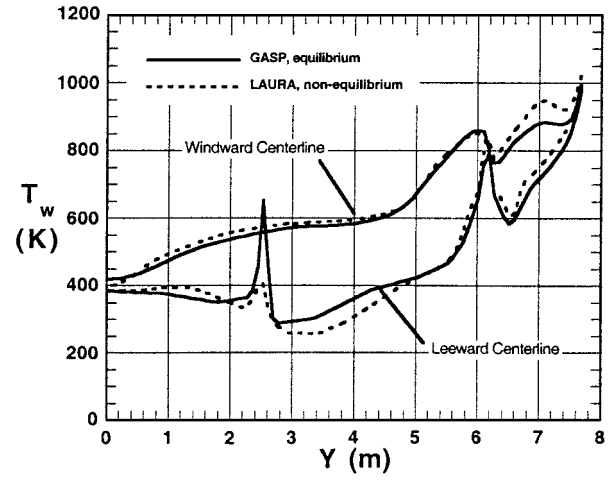

Fig. 37 Computed wall temperatures at $X = 15.0$ m (across the canted fins) for flight case 1, peak heating (Mach 8.82, $\alpha = 10$ deg).

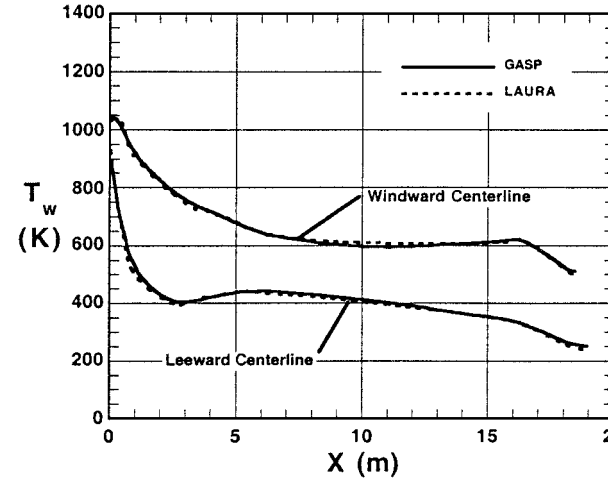

Fig. 38 Computed centerline wall temperatures for flight case 2 (Mach 8.89, $\alpha = 30$ deg).

turbulent boundary layer has not been resolved. The GASP computations are approximately 20% higher than the discrete trip data but are within ±10% of the bowed panel data.

Global Heating Comparisons

Graphical comparisons of GASP heating predictions and measured heating distribution for angles of attack of 20, 30, and 40 deg are presented in Figs. 25–30. In Figs. 25–30, wind-tunnel heating data, in the form of two-dimensional images obtained with the thermographic phosphor system, have been mapped onto the three-dimensional surface of the computational grid. This mapping permits direct comparisons of heating rates at all points on the body for which heating data have been obtained.

Windward surface views of the comparisons between GASP heating predictions and wind-tunnel data for angles of attack of 20, 30, and 40 deg are shown in Figs. 25–27, whereas front views for each case are shown in Figs. 28–30. In Figs. 25–30, gray indicates regions where no experimental data were obtained because that area of the vehicle was out of the field of view of the camera. In general, agreement between measured and predicted heating distributions appears good; although the GASP solutions exhibit higher heating along the chines, whereas the experimental data exhibit more sharply defined heating patterns for the shock interactions on the canted fins.

Bow-Shock/Flap-Shock Interaction

Several laminar GASP wind-tunnel computations with deflected +10- and +20-deg body flaps were also performed. Because the wind-tunnel data suggest that flow over the deflected body flaps is transitional/turbulent even at relatively low Reynolds numbers, comparisons with these laminar computations are not shown, although computed aerodynamic coefficients for these cases are compared with experimental data in Ref. 9. Although heating comparisons are not appropriate, an interesting inviscid phenomena can be discussed. The computations revealed the existence of an interaction at high angles of attack between the bow shock and the shock created by a deflected body flap. The wave system created by this interaction is illustrated by the pressure contours in Fig. 31, and the effects on the (laminar) body flap heating distributions are shown in Fig. 32. The expansion fan produced by the interaction impinges on the body flap, which causes a large increase in the heating on the trailing edge of the body flap. The wind tunnel data[10] suggest that the actual effect is even more severe owing to the turbulent nature of the body flap flow. Also, as discussed in Ref. 9, the drop in surface pressure caused by the expansion fan leads to a decrease in the pitching-moment contribution of the body flaps.

Flight Computations

Aeroheating predictions were made at two points along the Michael 9A-8 trajectory using GASP and LAURA. Note that

case 1 corresponds to the peak heating point along the trajectory. GASP computations were performed with a laminar, equilibrium air model, and LAURA computations were performed with a laminar, nonequilibrium air model.

As a result of the grid resolution study presented earlier, it was decided that a lower density grid ($64 \times 91 \times 65$) could be employed for the laminar GASP computations, although the LAURA computations had already been performed on the ($254 \times 181 \times 65$) grid. Also, because flap deflections for flight were not yet known at the time of work, the flaps were omitted from the computations. Both grids were rescaled to full-size for these computations.

Windward wall temperature distributions from these computations are presented in Figs. 33 and 34. Wall temperature distributions along centerline and axial stations for case 1 are plotted in Figs. 35–37, and centerline wall temperature distributions for case 2 are shown in Fig. 38.

The global comparisons for cases 1 and 2 suggest good agreement between the GASP and LAURA computations. The line-cut comparisons show that the two solutions agree to within less than $\pm 10\%$ except on parts of the centerline toward the end of the fuselage and on the leeward side of the canted fins. Because very close agreement was obtained on the nose, where any nonequilibrium effects would be greatest, the differences on the fins and toward the end of the body are likely due to the lower grid density used in the streamwise and tangential directions for the GASP computations rather than chemistry effects. The denser grid LAURA computation for case 1 also reveals shock interactions on the canted fins that are not present in the GASP computation.

Summary

As part of the X-33 thermal protection system development program, computational aeroheating solutions for the X-33 phase II vehicle were generated using two Navier–Stokes codes and an engineering code to complement wind-tunnel testing at NASA LaRC. Solutions were generated for Mach 6 wind-tunnel test cases and for two points along a representative flight trajectory. Laminar wind-tunnel and flight computations were performed using the Navier–Stokes solvers GASP and LAURA, and the LATCH boundary layer code was also used for wind-tunnel computations. Additional turbulent wind-tunnel cases were computed using GASP.

For the wind-tunnel cases, comparisons with experimental data were made along the X-33 windward centerline and at several axial locations. The laminar GASP and LAURA results were within the estimated $\pm 15\%$ uncertainty of the laminar data at all points and generally compared to within less than $\pm 10\%$. LATCH comparisons at axial stations were generally within the experimental uncertainty of the data, but the LATCH centerline results agreed with the data only on the first one-third of the vehicle. Turbulent GASP computations performed with the pressure-gradient correction to the Baldwin–Lomax[19] model tended to overpredict the experimental data by approximately 10% to 20%, which is slightly more than the experimental uncertainty. For the flight cases, GASP and LAURA predictions were found to agree to within less than $\pm 10\%$, except on the leeside of the canted fins and on the centerline toward the end of the vehicle.

Acknowledgments

The authors wish to offer thanks to several NASA Langley Research Center researchers who assisted in this work: Chris Riley for generating the LAURA inviscid flowfield solutions used in the LATCH computations, Ron Merski for providing support and development work for the IHEAT software used in the reduction and analysis of wind-tunnel phosphor data and three-dimensional mapping of the data; and Chris Glass and Michael Wright (of ELORET) for discussions on the use of the GASP code.

References

[1]Bekey, I., Powell, R., and Austin, R., "NASA Studies Access to Space," *Aerospace America*, Vol. 35, No. 5, 1994, pp. 38–43.

[2]Cook, S. A., "X-33 Reusable Launch Vehicle Structural Technologies," AIAA Paper 96-4563, Nov. 1996.

[3]Freeman, D. C., Jr., Talay, T. A., and Austin, R. E., "Reusable Launch Vehicle Technology Program," International Astronautical Federation, Paper IAF 96-V.4.01, Oct. 1996.

[4]Powell, R. W., Lockwood, M. K., and Cook, S. A., "The Road from the NASA Access-to-Space Study to a Reusable Launch Vehicle," International Astronautical Federation, Paper IAF-98-V.4.02, Sept. 1998.

[5]Baumgartner, R. I., and Elvin, J. D., "Lifting Body—An Innovative RLV Concept," AIAA Paper 95-3531, Sept. 1995.

[6]Hamilton, H. H., II, Weilmuenster, K. J., Berry, S. A., and Horvath, T. J., "Computational/Experimental Aeroheating Predictions for X-33 Phase II Vehicle," AIAA Paper 98-0869, Jan. 1998.

[7]Thompson, R. A., Hamilton, H. H., II, Berry, S. A., and Horvath, T. J., "Hypersonic Boundary Layer Transition for X-33 Phase II Vehicle," AIAA Paper 98-0867, Jan. 1998.

[8]Berry, S. A., Horvath, T. J., Hollis, B. R., Thompson, R. A., and Hamilton, H. H., II, "X-33 Hypersonic Boundary-Layer Transition," *Journal of Spacecraft and Rockets*, Vol. 38, No. 5, 2001, pp. 646–657.

[9]Hollis, B. R., Thompson, R. A., Murphy, K. J., Nowak, R. J., Riley, C. J., Wood, W. A., Alter, S. J., and Prabhu, R. K., "X-33 Aerodynamic Computations and Comparisons with Wind-Tunnel Data," *Journal of Spacecraft and Rockets*, Vol. 38, No. 5, 2001, pp. 684–691.

[10]Horvath, T. J., Berry, S. A., Hollis, B. R., Liechty, D. S., Hamilton, H. H., II, and Merski, N. R., "X-33 Experimental Aeroheating at Mach 6 Using Phosphor Thermography," *Journal of Spacecraft and Rockets*, Vol. 38, No. 5, 2001, pp. 634–645.

[11]Murphy, K. J., Nowak, R. J., Thompson, R. A., Hollis, B. R., and Prabhu, R., "X-33 Hypersonic Aerodynamic Characteristics," *Journal of Spacecraft and Rockets*, Vol. 38, No. 5, 2001, pp. 670–683.

[12]Thompson, R. A., "Review of X-33 Hypersonic Aerodynamic and Aerothermodynamic Development," 22nd International Congress of the Aeronautical Sciences, Rept. ICA-0323, Aug.–Sept. 2000.

[13]"GASP Version 3, The General Aerodynamic Simulation Program, Computational Flow Analysis Software for the Scientist and Engineer, User's Manual," AeroSoft, Inc., Blacksburg, VA, May 1996.

[14]Gnoffo, P. A., "An Upwind-Biased, Point-Implicit Algorithm for Viscous, Compressible Perfect-Gas Flows," NASA TP 2953, Feb. 1990.

[15]Cheatwood, F. M., and Gnoffo, P. A., "User's Manual for the Langley Aerothermodynamic Upwind Relaxation Algorithm (LAURA)," NASA TM 4674, April 1996.

[16]Hamilton, H. H., II, Greene, F. A., and DeJarnette, F. R., "Approximate Method for Calculating Heating Rates on Three-Dimensional Vehicles," *Journal of Spacecraft and Rockets*, Vol. 31, No. 3, 1994, pp. 345–354.

[17]Roe, P. L., "Approximate Riemann Solvers, Parameter Vectors and Difference Schemes," *Journal of Computational Physics*, Vol. 43, No. 2, 1981, pp. 357–372.

[18]Van Leer, B., "Flux Vector Splitting for the Euler Equations," *Proceedings of the 8th International Conference on Numerical Methods in Fluid Dynamics*, Springer-Verlag, Berlin, 1981.

[19]Baldwin, B. S., and Lomax, H., "Thin Layer Approximation and Algebraic Model for Separated Turbulent Flow," AIAA Paper 78-257, Jan. 1978.

[20]Yee, H. C., "On Symmetric and Upwind TVD Schemes," NASA TM 88325, 1990.

[21]Cooke, J. C., "An Axially Symmetric Analogue for General Three-Dimensional Boundary Layers," Ministry of Aviation, Aeronautical Research Council, Repts. and Memoranda 3200, London, 1961.

[22]Zoby, E. V., and Simmonds, A. L., "Engineering Flow Field Method with Angle-of-Attack Applications," *Journal of Spacecraft and Rockets*, Vol. 22, No. 4, 1985, pp. 398–405.

[23]Micol, J. R., "Hypersonic Aerodynamic/Aerothermodynamic Testing Capabilities at Langley Research Center: Aerothermodynamic Facilities Complex," AIAA Paper 95-2107, June 1995.

[24]Alter, S. J., "Grid Generation Techniques Utilizing the Volume Grid Manipulator," AIAA Paper 98-3012, June 1998.

[25]Alter, S. J., "The Volume Grid Manipulator (VGM): A Grid Reusability Tool," NASA CR-4772, April 1997.

[26]Harten, A., "High Resolution Schemes for Hyperbolic Conservation Laws," *Journal of Computational Physics*, Vol. 49, No. 3, 1983, pp. 357–393.

[27]Prabhu, D. K., Wright, M. J., Marvin, J. J., Brown, J. L., and Venkatapathy, E., "X-33 Aerothermal Design Environment Predictions: Verification and Validation," AIAA Paper 2000-2686, June 2000.

[28]Roe, P. L., "Some Contributions to the Modelling of Discontinuous Flows," *Proceedings of the 1983 AMS–SIAM Summer Seminar on Large Scale Computing in Fluid Mechanics*, Vol. 22, Lectures in Applied Mathematics, Society for Industrial and Applied Mathematics, Philadelphia, 1985, pp. 163–193.

[29]Chakravarthy, S. R., and Osher, S., "High Resolution Applications of the Osher Upwind Scheme for the Euler Equations," AIAA Paper 83-1943, 1983.

[30]Merski, N. R., "Global Aeroheating Wind-Tunnel Measurements Using Improved Two-Color Phosphor Thermography Method," *Journal of Spacecraft and Rockets*, Vol. 36, No. 2, 1999, pp. 160–170.

[31]Berry, S. A., Horvath, T. J., DiFulvio, M., Glass, C. E., and Merski, N. R., "X-34 Aeroheating at Mach 6 and Mach 10," AIAA Paper 98-0881, Jan. 1998.

[32]Fay, J. A., and Riddell, F. R., "Theory of Stagnation Point Heat Transfer in Dissociated Air," *Journal of Aeronautical Sciences*, Vol. 15, No. 2, 1958, pp. 73–85.

[33]Gupta, R. N., Lee, K. P., Zoby, E. V., Moss, J. N., and Thompson, R. A., "Hypersonic Viscous Shock-Layer Solutions over Long Slender Bodies, Part 1: High Reynolds Number Flows," *Journal of Spacecraft and Rockets*, Vol. 27, No. 2, 1990, pp. 175–184.

[34]Cheatwood, F. A., and Thompson, R. A., "The Addition of Algebraic Turbulence Modeling to Program LAURA," NASA TM 107758, April 1993.

[35]Hollis, B. R., Horvath, T. J., Berry, S. A., Hamilton, H. H., II, and Alter, S. J., "X-33 Computational Aeroheating Predictions and Comparison with Experimental Data," AIAA Paper 99-3559, 1999.

T. C. Lin
Associate Editor

Color reproductions courtesy of NASA Langley Research Center.